Published in final edited form as:

J Elast. 2021 August ; 145(1-2): 295–319. doi:10.1007/s10659-021-09843-7.

A Hybrid Microstructural-Continuum Multiscale Approach for Modeling Hyperelastic Fibrous Soft Tissue

Maryam Nikpasand[1], **Ryan R. Mahutga**[2], **Lauren M. Bersie-Larson**[2], **Elizabeth Gacek**[2], **Victor H. Barocas**[2,*]

[1]Department of Mechanical Engineering, University of Minnesota – Twin Cities, Minneapolis, MN, USA

[2]Department of Biomedical Engineering, University of Minnesota – Twin Cities, Minneapolis, MN, USA

Abstract

The heterogeneous, nonlinear, anisotropic material behavior of biological tissues makes precise definition of an accurate constitutive model difficult. One possible solution to this issue would be to define microstructural elements and perform fully coupled multiscale simulation. However, for complex geometries and loading scenarios, the computational costs of such simulations can be prohibitive. Ideally then, we should seek a method that contains microstructural detail, but leverages the speed of classical continuum-based finite-element (FE) modeling. In this work, we demonstrate the use of the Holzapfel-Gasser-Ogden (HGO) model [1, 2] to fit the behavior of microstructural network models. We show that Delaunay microstructural networks can be fit to the HGO strain energy function by calculating fiber network strain energy and average fiber stretch ratio. We then use the HGO constitutive model in a FE framework to improve the speed of our hybrid model, and demonstrate that this method, combined with a material property update scheme, can match a full multiscale simulation. This method gives us flexibility in defining complex FE simulations that would be impossible, or at least prohibitively time consuming, in multiscale simulation, while still accounting for microstructural heterogeneity.

* baroc001@umn.edu, Phone: 612-626-5572, Fax: 612-626-6583, 7-105 Nils Hasselmo Hall, 312 Church St SE, Minneapolis, MN, 55455.

Authors' contributions

MN and VHB conceived the initial idea for this work. MN, RRM, LMBL, and EG performed the research. MN, RRM, LMBL, EG, and VHB prepared and edited the manuscript.

Conflicts of interest/Competing interests

The authors declare no conflicts of interest.

Ethics approval

Not applicable.

Consent to participate

Not applicable.

Consent for publication

Proper consent has been obtained from all applicable parties.

Availability of data and material

All raw data are available from the contact author upon request.

Code availability

The codes, simulations, and models used in this work are available on GitHub.

Keywords

Fiber network; multiscale biomechanics; facet capsular ligament; artery; HGO model

1. Introduction

Biological soft tissues are complex, hydrated composites, typically simplified as a mixture of fibrous proteins (primarily collagen and elastin) and cells [3, 4]. The multi-constituent nature of tissues and the dependence on crimped collagen fibers to add structural reinforcement makes tissue mechanical behavior inherently nonlinear. The heterogeneous distribution of constituents due to the varied mechanical loading environments, and the various microstructural requirements of cell populations also tend to make tissues anisotropic (Fig. 1). The behavior of these tissues, including dissonant behavior from tissue to tissue (e.g. auxetic behaviors in tendon/ligaments [5, 6] compared to the relative rubber-like behavior of arteries [7–11]), makes defining a consistent constitutive model challenging.

Despite the complexity of tissue microstructure, a number of models have been proposed in the continuum framework to define the nonlinear, anisotropic material behavior. By far the most common method for defining the nonlinearity of soft tissues is by treating the material as having stress developed as an exponential of strain [1, 12–16]. Perhaps the most significant, and widely used constitutive model for nonlinear, anisotropic materials is the Holzapfel-Gasser-Ogden (HGO) model [1, 2]. The beauty of this model is in its simplicity, its broad applicability [17–28], and its adaptability and ability to be extended [20, 29–34]. In its most basic form, the model is described by a strain energy density function of a neo-Hookean ground substrate with an exponential anisotropic fiber component. The HGO model is given by:

$$W = W^m + W^f = C_1(I_1 - 3) + C_2/(2C_3)[\exp(C_3(I_4 - 1)^2) - 1] \quad \text{Eq. 1}$$

where W^m is the non-fibrillar matrix strain energy density, W^f is the fiber strain energy density, C_1 is the neo-Hookean material parameter, $I_1 = C_{II}$ is the first strain invariant of the right Cauchy-Green tensor (C_{IJ}), C_2 is the fiber modulus term, C_3 is the fiber nonlinearity, and $I_4 = a_I^0 C_{IJ} a_J^0$ is the fourth strain invariant of the right Cauchy-Green tensor C_{IJ} and $\boldsymbol{a^0}$ is a vector describing the fiber direction.

A critical simplification in the analysis of such tissue behavior is the assumption that the deformation of the underlying fiber network is affine [35]. This assumption has been used countless times to lead to different soft tissue models based on invariants and/or the complete fiber distribution. However, the detailed microstructural behavior of a tissue is not, in general, affine [36, 37]. This fact leads to the use of multiscale models where one can precisely define the microstructure while still leveraging the advantages of finite-element modeling [38–50]. Of course, the necessity of solving many microstructural problems in the pursuit of modeling the deformation of a specific tissue leads to a huge computational cost. This computational cost is especially exacerbated when one adds in multi-physics such as tissue failure, fluid dynamics, or microstructural remodeling [22, 24, 25, 51–63]. Thus, the

ideal scenario would be to use the microstructural models when we need the structural and mechanical detail, but use a constitutive model (like the HGO) with a finite element solver when we need to run large-scale, multi-physics models.

In this work, we propose a hybrid modeling approach in which we fit an HGO model to deformations imposed on a microstructural element, then use the HGO constitutive model to enhance the speed of the finite element simulation. This technique allows one to examine microstructural features when necessary without generating and solving all the microstructural problems during the finite element solution. In this way, we enhance the flexibility in multiscale modeling by allowing for the use of larger domains with heterogeneous material definitions and complex boundary conditions without the need to run computationally expensive fully coupled multiscale simulations via a supercomputer.

2. Methods

2.1 Mechanics Mathematical Preliminaries

Kinematic quantities important in the following analysis are given here. The first important descriptor is the deformation gradient, $\boldsymbol{F}$, which maps the deformation from the undeformed domain to the deformed domain. Out of the deformation gradient comes the Jacobian, $\boldsymbol{J}$ which is given as the determinant of $\boldsymbol{F}$, and represents the volume change due to the deformation. Additional important kinematic variables are the right Cauchy-Green tensor $\boldsymbol{C}$, defined by $C_{IJ} = F_{kI}F_{kJ}$, and the Green-Lagrange strain tensor $\boldsymbol{E}$, defined by $E_{IJ} = \frac{1}{2}(C_{IJ} - \delta_{IJ})$ where δ_{IJ} is the Kronecker delta. In this work, we also use several strain invariants. The isotropic first strain invariant, $I_1 = C_{II}$, and the transverse isotropic fourth strain invariant, $I_4 = a_I^0 C_{IJ} a_J^0$, dictated by a direction vector, $\boldsymbol{a^0}$. We further define the fourth strain invariant as the square of the averaged fiber stretch $\langle I_4 \rangle = H_{IJ}C_{IJ} = \hat{\lambda}_f^2$, where H_{IJ} is the generalized structure tensor (defined below) and $\hat{\lambda}_f$ is the averaged fiber stretch. A number of mechanics quantities are also addressed in the following analysis. The first is the concept of stress. The Cauchy stress carries the physical interpretation of force per current cross-sectional area and is defined as $\boldsymbol{\sigma} = \frac{2}{J}\boldsymbol{F}\frac{\partial W}{\partial C}\boldsymbol{F}^T$ where W is the strain energy density function for the material. The second Piola-Kirchoff stress is defined $\boldsymbol{S} = \frac{\partial W}{\partial \boldsymbol{E}} = \boldsymbol{J}\boldsymbol{F}^{-T}\boldsymbol{\sigma}\boldsymbol{F}^{-1}$, which carries no meaningful physical interpretation, but does represent a useful quantity for purposes of calculation due to both force and area being mapped to the reference configuration.

2.2 Methodological Principles

Our goal is to convert a discrete fiber network model, which allows a high degree of structural fidelity but is computationally intensive, into an HGO model, which is computationally much more tractable. Because our goal is computational simplicity, we use the simple form of the HGO model shown above in Eq. 1. It is routinely assumed in affine models of this type that the constitutive equation can be written in terms of independent contributions from a non-fibrous matrix and the fiber network. The non-fibrous matrix is often incompressible or includes a volume-dependent term to limit material compressibility.

Similarly, in multiscale models [43–45], a separate neo-Hookean matrix is introduced in parallel to the network. For the present analysis, it is therefore assumed that the fiber network contribution is distinct from the neo-Hookean, incompressible non-fibrillar matrix, and the current work focuses on the fiber network contribution only. The fundamental challenge to be addressed is to convert a fiber network model into one based on the fiber stretch via I_4 (i.e. $a_I^0 C_{IJ} a_J^0$ in a model of the classical HGO form). That is, the problem is to determine parameters C_2 and C_3 such that the model

$$W^f = C_2/(2C_3)[exp(C_3(\langle I_4\rangle - 1)^2) - 1] \quad \text{Eq. 2}$$

yields a fiber-network strain energy density function W^f that matches the results from the network computations. Here we delineate the difference between the square stretch, I_4, in a given direction $\boldsymbol{a^0}$, and the square stretch in the average fiber direction $\langle I_4\rangle = H_{IJ}C_{IJ}$. The invariant $\langle I_4\rangle$ is calculated as the double contraction of a generalized structure tensor H_{IJ} with the right Cauchy-Green tensor C_{IJ}. The generalized structure tensor H_{IJ} is defined as

$$H_{IJ} = \frac{1}{V}\int_\Omega N_I^m N_J^m dV = \frac{\sum_{m=1}^k V^m N_I^m N_J^m}{\sum_{m=1}^k V^m} \quad \text{Eq. 3}$$

where $\boldsymbol{N}^m$ is the unit vector in the direction of fiber m, and $V^m = \pi(R^m)^2 L^m$ is the volume of a fiber with radius, R^m and length, L^m. The calculation of the generalized structure tensor and its use to calculate $\langle I_4\rangle$ are based on the underlying assumption that, in general, the network behaves affinely. This calculation does not account for different properties of fibers such as the tension-compression asymmetry of fiber response, or the different fiber types that might occur (e.g., collagen and elastin). There are also differences incurred because the fibers are exponential and the deformation in a network is not affine, meaning the apparent modulus of any given fiber need not be the same as any other or, in fact, the average fiber. There are several ways one could approach this problem, including calculating the end-state $h_{ij} = F_{iK}H_{KL}F_{jL}$ for the network and mapping it back to the undeformed domain with or without those fibers that are in compression. This strategy, however, would rely on an accurate representation of the deformation, which is often unknown *a priori*. A second option would be to not calculate the structure tensor from the fiber network, but instead treat its components as additional fitting parameters. Doing so, however, would leave the underlying structural information we have from the microstructural networks unutilized.

One of the challenges with a structure-tensor-based model is the so-called tension-compression switch. Fibers are very stiff in tension but buckle and support almost no load in compression. If the structure tensor and the resulting calculated $\langle I_4\rangle$ do not exclude fibers in compression, then the model is at risk of overpredicting the stress response, especially if the model has been fitted to data from a different strain field. This issue has received much discussion (e.g., [30, 64]), and variations have been proposed in which compressed fibers are excluded [31, 34]. In the current work, we chose to use a simpler, all-fiber structure tensor. As noted earlier, the tension-compression switch is approximated smoothly in the discrete-fiber model by the exponential fiber constitutive equation; the specific representation of the switch has relatively little effect on the overall network mechanics [36]. We refer the

reader to the in-depth discussions on structure tensors and tension-compression asymmetry in biological tissues given in other works [34, 64, 65].

There are, of course, infinitely many possible deformations, but the fitting problem can be reduced conveniently by considering the fiber network strain energy W^f as a function of $\hat{\lambda}^f = \sqrt{\langle I_4 \rangle} = \sqrt{\mathrm{H_{IJ}C_{IJ}}}$, which represents an averaged fiber stretch in the affine, continuous model. Although the product $\mathrm{H_{IJ}C_{IJ}}$ does not have any physical meaning within the context of the non-affine discrete fiber model, it is easily calculated and convenient for use in the fitting process. Likewise, W^f can be calculated either from computing an average stress in the domain [66] and integrating it with respect to its energy conjugate in the continuum sense to determine a strain energy, or by summing the total strain energy of all fibers and dividing by the domain volume. These two methods are given by

$$W^f = \int_{E_{IJ}=0}^{E_{IJ}} S_{IJ} dE_{IJ} = \frac{1}{V}\int_{\Omega} w^m dV \approx \frac{1}{V}\sum_{m=1}^{k} w^m V^m \qquad \text{Eq. 4.1}$$

where W^f is the total strain energy density of the fiber network, S_{IJ} is the second Piola-Kirchhoff stress, E_{IJ} is the Green strain, w^m is the strain energy density of fiber m, V is the domain volume, and V^m is the volume of fiber m. The individual strain energy of a fiber is given by

$$w^m = \int_{E_{IJ}^m=0}^{E_{IJ}^m} S_{IJ}^m dE_{IJ}^m \qquad \text{Eq. 4.2}$$

The results from a network simulation of any macroscopic deformation can then be represented as W^f vs. λ^f. This method is further summarized in the flowchart in Fig. 2. With W^f vs. λ^f from the network determined, the total-fiber constitutive law can be fit to the aggregated network-scale simulation results. Although in principle any total-fiber constitutive law could be used, a continuum model in an exponential format that is similar to the fiber's qualitative behavior is an intuitive choice to predict fibers' overall behavior. Therefore, throughout this work we use the expression of Eq. 2 and fit C_2 and C_3 to the W^f vs. λ^f curve.

2.3 Case Study: Multiple Deformations of a Single Network

To verify the ability of an HGO-type model to reproduce network mechanical response, a moderately aligned (H_{11} = 0.69, H_{22} = 0.21 and H_{33} = 0.10) 3D Delaunay network was generated using the Delaunay triangulation function, *delaunay*, in MATLAB (R2019a, MathWorks, Natick, MA). This alignment was chosen due to the tendency of collagenous tissues to possess a preferred alignment, observed in, for example, ligaments [67, 68]. Briefly, randomly generated seed points in the 3D space were used to generate a Delaunay tetrahedral network. The seed points represent network nodes, and the edges of the tetrahedral regions represent the fibers. After initial generation, the network was subjected to artificial stretches to reach the desired alignment. Finally, the aligned network was clipped from the stretched network to a unit cube, and the fibers and nodes inside the cube were

extracted to form the aligned networks used in these simulations. This process was done iteratively, with the number of the seed points adjusted in order to obtain a final volume fraction of 0.04 for each network, holding the fiber cross-sectional areas constant. This fiber fraction represents a collagenous tissue as in [69, 70]. The fiber volume fraction in a network is given by

$$\phi^f = \frac{V^f}{V} = \frac{\chi \sum_{m=1}^{k} \pi (R^m)^2 L^{*m}}{\chi^3 V^*} \quad \text{Eq. 5}$$

where ϕ^f is the fiber volume fraction, V^f is the total fiber volume, V is the network volume, χ is a scale factor converting from computational length units to real length unit [m], R^m is the radius of fiber m, L^{*m} is the length of fiber m in computational space, and V^* is the network volume in computational space.

The fibers in these networks were then modeled as one-dimensional nonlinear springs connected at freely-rotating pin joints (nodes) at two ends. The slender fibers are subjected to moderate to large strains and have negligible bending stiffness. The governing equation describing the *fibers in the network* was adapted from [71] and is defined as

$$f = \frac{kA}{B}(exp[BE] - 1) \quad \text{Eq. 6}$$

where f is the force generated within the fiber, A is the fiber undeformed cross-sectional area, k and B are constant and represent fiber stiffness and nonlinearity, respectively, and $E = \frac{1}{2}\left(\lambda_m^2 - 1\right)$ is the Green strain of the fiber, m, stretched to stretch ratio λ_m. The values for k and B in Eq. 6 and the fiber radius were set to 10 MPa, 2.5, and 100nm, respectively, following Dhume et al. [69]. We emphasize that the function in Eq. 6 represents a single fiber in the network, where the function itself is chosen so that the force is zero at zero strain, with large magnitude forces developed in tension and low magnitude forces developed in compression, simulating the tension-compression switch seen in native collagen fibers. The solution of the network state given a prescribed deformation was calculated using Newton iteration to balance all forces on internal nodes. The overall Cauchy stress state for the network was then calculated as

$$\sigma_{ij} = \frac{1}{V}\int_{\Omega} \sigma_{ij} dV \approx \frac{1}{V}\sum_{m=1}^{k} \sigma_{ij}^m V^m = \frac{1}{V}\sum_{m=1}^{k}\left(\frac{f_i^m}{A^m}\right) n_j^m (A^m l^m) = \frac{1}{V}\sum_{m=1}^{k} f_i^m n_j^m l^m \quad \text{Eq. 7}$$

where σ_{ij} is the network volume averaged Cauchy stress, V is the network volume, σ_{ij}^m is the Cauchy stress of fiber m, V^m is the volume of fiber m, f_i^m is the force from fiber m, A^m is the instantaneous cross-sectional area of fiber m, $\boldsymbol{n^m}$ is the fiber normal direction in the deformed state, and l^m is the current length of fiber m.

The network was subjected to five different deformations: x-direction uniaxial stretch, simple shear on the xy- and yz-faces, and equibiaxial stretch in the xy- and xz-plane

(Fig. 3a, b). The network underwent a stretch of 1.8 in the x-direction. The stretches for other deformations were calculated such that the final $\hat{\lambda}_f = \sqrt{H_{IJ}C_{IJ}}$ in all deformations was equal to the calculated $\hat{\lambda}_f$ for the x-direction uniaxial stretch experiment. These deformations were selected because the network of interest has $H_{11} > 0.33$, meaning that the main fiber direction falls mostly in the x-direction. This approach ensures $H_{IJ}C_{IJ} > 1$, which allows for proper fitting of the W^f curves. In this work, the directionality of the networks drove the deformations used for the initial HGO fits (i.e. networks aligned in x are subjected to x, xy, and/or xz deformations). For each deformation, the boundary nodes were displaced, and internal node equilibrium was attained using Newton iteration. In all deformations, the boundaries were displaced such that incompressibility was guaranteed on the network's bounding box. For each deformation, the (macroscopic) right Cauchy-Green tensor, C_{ij}, and the macroscopic volume-averaged Cauchy stress, σ_{ij}, were calculated and stress converted to W^f vs. λ^f as described previously (Eq. 4). The W^f vs. λ^f curves were plotted simultaneously for all the generated deformations, and a single constitutive HGO fiber model given in Eq. 2 was fit to the data using MATLAB (R2019a, MathWorks, Natick, MA) built in constrained minimization routine *fmincon*. An example of the W^f vs. λ^f curves and the fit are shown in Fig. 5.

To show that how fiber realignment can differ in various deformations, the largest eigenvalue of the instantaneous orientation tensor at each steps, h_{ij}, was calculated and plotted vs. the average value of fiber stretch (Fig. 3c, d).

2.4 Alignment Dependence for Delaunay Networks

We evaluated the proposed method by generating HGO model parameters for 750 Delaunay networks with a range of alignments. The various deformations described in Fig. 3 were imposed on the networks, and W^f vs. λ^f plots were constructed for each deformation. For each network, the W^f vs. λ^f deformation plots were fit together with the single HGO model given in Eq. 2. Contour plots of the material parameters were then created to evaluate the material property variation with alignment and assess if the HGO model could be broadly applied across Delaunay networks of varying alignment.

2.5 Hybrid Microstructural-Continuum Multiscale Approach

The novelty of this approach is that it removes much of the computational overhead needed in fully coupled multiscale approaches. Particularly, the use of the network model to fit a continuous material model (HGO) lets us leverage the increased speed in calculating both stress and the material (or spatial) elasticity tensor of the continuum material model over the micro-network model. Take, for example, a network consisting of Q fibers and R nodes where we have Cauchy stress given by Eq. 7 converted to the PK2 stress to calculate the material elasticity tensor

$$C_{IJMN} = \frac{\partial S_{IJ}}{\partial C_{MN}} = \frac{\partial}{\partial C_{MN}}\left[\frac{1}{V_0}F^{-1}_{Im}\left(\sum_{k=1}^{Q} f^k_m l^k n^k_n\right)F^{-1}_{Jn}\right] \quad \text{Eq. 8}$$

where S_{IJ} is the network PK2 stress, and C_{MN} is the right Cauchy-Green tensor, V_0 is the undeformed network volume, $\boldsymbol{F}^{-1}$ is the inverse deformation gradient tensor, $\boldsymbol{f}^{\boldsymbol{k}}$ is the

fiber force vector, $\boldsymbol{n^k}$ is the fiber direction vector, and l^f is the fiber current length. If we examine these equations, it becomes clear that, at a minimum, we would need to calculate the fiber force, $\boldsymbol{f}$ for each fiber, k, and we would need to calculate something akin to the fiber elasticity, $\frac{\partial}{\partial C_{MN}}\left(\left(\sum_{k=1}^{N} f_m^k l_n^k\right)\right)$ for each fiber, k. For each network at each Gauss point in each element (i.e. 8 networks per hex element), we would have to calculate both of these quantities. That means we would have to run one network simulation per Gauss point and make Q calculations for the stress and Q calculations for the elasticity per network, if there existed an analytical solution to the elasticity tensor, which, in the case of non-affine networks, is not necessarily the case. Additionally, the network solution relies on determining the static force balance of internal nodes, which, if solved explicitly, would yield another R calculations. However, this solution typically involves implicit solution via Newton iteration, resulting in between 5–10 iterations to achieve static equilibrium for a well-conditioned network. Thus, in the best case scenario, we would have $2Q+R$ calculations per Gauss point. If we contrast this with the HGO model, which involves one stress calculation and one elasticity calculation per Gauss point, we expect a minimum decrease in computational cost of $Q+\frac{1}{2}R$ per network. The overall computation time is presented in Table 1.

One can fit the behavior of a network by subjecting it to many potential deformations and fitting the total data (as in Case Study 2.3), or one could simply fit one single deformation of interest. The former will give a better rough estimate if the actual deformation of the material is unknown, while the latter will be more accurate if there is confidence in the magnitude and type of deformation the network will undergo. We henceforth refer to the initial average fit to many deformations as the ***HGO fit*** and to the later fit to a single deformation as the ***refit***. Care must be taken when refitting to a single deformation, as not all deformations will cause the average stretch to be greater than one. In these cases, the fit will not capture the behavior of the network, and an alternative fit should be used. In our model, we use two methods for dealing with this issue: 1. If the average stretch never exceeds one, we simply make the fiber modulus zero, thereby removing the fiber contribution, and 2. If the average stretch does eventually exceed one, but the fit is poor due to the behavior of the strain energy curve (i.e., Fig. 4), we attempt to fit only the slope of the strain energy curve for which the average stretch is greater than one. This effectively allows us to fit something closer to the stress, as the stress is directly related to the slope of the W^f vs. λ^f curve.

Once the HGO properties are fitted to the network simulations, we can use those material inputs in a finite element (FE) framework as shown in Fig. 4a. This allows us to rely on the constitutive relation to solve the FE simulation rather than having to use costly microscale network simulations. Further, once we have the solution from the FE simulation, we can extract the deformation gradient at any point of interest and run the networks to evaluate any microstructural quantities such as fiber orientation or fiber stresses. This offers us the ability to evaluate discrete quantities in regions of interest, or to pass strains down to the microstructure to evaluate fiber remodeling or failure.

In an FE simulation, one often is concerned with an imposed deformation that occurs in a series of small steps. In this case, one can choose whether to iterate at a given step until

the deformation field and model are consistent, or to adjust the model based on a given step and use the updated parameters for *the next* step. The latter approach introduces some error in that the continuum model does not match the microscopic model at the end of the step, but it has the considerable efficiency advantage of allowing an update at relatively low computational cost. The lagging update errors can also be further mitigated by imposing smaller deformation steps where in the limit of an infinitesimally small step the error becomes zero. If one only cared about the end state of the deformation, then this method would introduce little error, especially if the state or states of interest are iterated to match microscopic and macroscopic stress. For this work, we chose the less costly approach of allowing the continuum model correction to proceed with the previous step update, and only iterate the state of interest, which in our example (2.7) is the final step. This process is shown in Fig. 4b.

2.6 Case Study: Single-Network Model Performance for Non-Fitted Deformation

In this study, we compared the fit of the HGO model to an array of deformations and the fit of an HGO model to a specific deformation. To do this, we first fit the network to x-uniaxial (magnitude 1.25), xy-biaxial, xz-biaxial (magnitude 1.1), xy- shear and xz-shear (magnitude 0.15). Once the HGO model had been fit, we tested it on a deformation that differed from the ones used in fitting the model parameters. Specifically, we modeled an element from complex motion of the stretching and three-point bending of a facet capsular ligament as in [72]. We imposed the deformation gradient of an element experiencing maximum stretch during the simulated experiment:

$$\boldsymbol{F} = \begin{bmatrix} 1.239 & 0 & 0.0035 \\ 0 & 1.048 & -0.0014 \\ -0.0080 & 0.102 & 0.770 \end{bmatrix} \quad \text{Eq. 9}$$

which was dissimilar to the uniaxial, biaxial, and shear deformations used to fit the initial HGO model. The deformation was imposed on the discrete network model, and the volume-averaged Cauchy stress was determined. Concurrently, the Cauchy stress was calculated by the HGO model using the parameters fitted to the suite of deformations (given above as ***HGO fit***). In addition, in keeping with the ***refit*** update strategy discussed above, after the simulation was done, we refit the HGO model to W^f vs. λ^f giving us stress estimates for the deformation imposed in Eq. 9.

2.7 Comparison between Network-to-HGO Model and Full Multiscale Model

The goal of the proposed method is to facilitate higher-efficiency multiscale simulations based on network structure. To evaluate its potential, we performed a full multiscale simulation of a representative L4-L5 facet capsular ligament (FCL) sample during spinal flexion (reproducing the model of Zarei et al. [73]). The model boundary conditions are defined through application of nodal displacements based on the bone surface from the kinematic simulation of Bermel et al. [74]. Additional details of the simulation setup are available in [73]. The same micro-networks used in [73] were applied in the network-to-continuum scheme, and the resulting continuum biomechanics problem was solved using the open-source finite-element platform FEBio [75]. Because FEBio does not support the HGO

model, the ligament was modeled as a coupled solid mixture of a Mooney-Rivlin (effectively reduced to a neo-Hookean) ground matrix with three fiber families, leading to the strain energy density function

$$W = W^m + W^f \quad \text{Eq. 10A}$$

where W is the total strain energy density. The first term in the total strain energy density is the non-fibrillar matrix component of the strain energy density W^m given by

$$W^m = C_1(I_1 - 3) - 2C_1 \ln J + \frac{\lambda}{2}(\ln J)^2 \quad \text{Eq. 10B}$$

where C_1 is half the second Lamé parameter relating to the neo-Hookean material parameter, I_1 is the first strain invariant of the right Cauchy-Green tensor, C_{IJ}, $J = \det(\boldsymbol{F})$ is the differential volume change of the deformation, and λ is the first Lamé parameter relating to the bulk modulus. The tissue was considered as a compressible material with a matrix modulus and bulk modulus that matched those used by Zarei et al. [73]. The compressibility of the FCL was experimentally observed by Little et al., who suggest that the Poisson's ratio is as low as 0.3 [67]. The second half of the strain energy density is the fiber component of the strain energy density W^f given by

$$W^f = C_2/(2C_3)\sum_{p=1}^{3} h^p\left(exp(C_3(I_4^p - 1)^2) - 1\right) \quad \text{Eq. 10C}$$

where C_2 represents the fiber modulus, C_3 captures fiber nonlinearity, h^p is the weighting factor for fiber family p, $I_4^p = C_{IJ}N_I^pN_J^p = (\lambda^p)^2$ is the fourth strain invariant of the right Cauchy-Green tensor, C_{IJ}, $\boldsymbol{N}^p$ is the unit vector pointing in the direction of fiber family p in the undeformed state, and λ^p is the average fiber stretch of fiber family p. The undeformed direction vectors $\boldsymbol{N}^p$, were generated directly from the structure tensors H_{IJ} by taking the eigenvectors, which, since H_{IJ} is a symmetric positive definite matrix, give three orthogonal fiber directions. For the current work, we use these three orthogonal fiber families pointing in the principal directions of H_{IJ} and assign the weight h^p to each family based on the eigenvalues of H_{IJ} corresponding to each eigenvector $\boldsymbol{N}^p$. Fiber material parameters C_2 and C_3 were fit to the W^f vs. λ^f plots using the method described above. The neo-Hookean material parameter, C_1, and the bulk modulus parameter, λ, were set to 0.025 MPa and 0.417 MPa, respectively, to match [73]. The analogous stress for this strain energy function can be found in the FEBio manual [76] under compressible materials Fiber with Exponential Power Law (4.1.3.8) and Coupled Mooney-Rivlin (4.1.3.17).

Briefly, to generate the finite-element simulation, we imported the L4-L5 FCL geometry mesh of hexahedral elements [73], and applied HGO parameters to each individual element corresponding to the microstructural networks applied in [73]. To simulate flexion, the displacement of the nodes at the entheses (left and right sides of Fig. 4a) were specified based on the the L4-L5 motion segment model [74] as further described in [73].

Initially, micro-networks from the full multiscale model were fit to the HGO using multiple deformations, as described previously. A FEBio model of the representative FCL sample

bending in flexion was then simulated using the initial HGO fit for fiber material parameters in Eq. 7. For added accuracy, the deformation gradient tensor for each element in the FEBio HGO model was then used to refit the fiber material parameters. For comparison, maximum shear stress and maximum shear strain fields were computed for the full multiscale model, the FEBio initial HGO model, and the FEBio refit HGO model.

3. Results

3.1 Multiple Deformations of a Single Network

A representative fiber network was chosen for detailed analysis. The network is shown after moderate (10% Green strain, Fig. 3a) and extremely large (112% Green strain in Fig. 3b) deformations. The deformed network is shown for x-uniaxial, xy- and xz-shear, and xy- and xz-biaxial deformations (Fig. 3a and 3b). In this case, the network of interest has $H_{11} = 0.69$, meaning that the use of x-direction deformations ensures $H_{IJ}C_{IJ} > 1$ which allow us to more accurately fit the W^f curves.

The largest eigenvalue of the instantaneous orientation tensor, h_{ij}, is plotted versus the average value of fiber stretch over the full stretch range (Fig. 3c) and in close-up of the small-stretch range (Fig. 3d). The eigenvalues show large variation with deformations which is particularly pronounced at low strains. This result shows that the fiber realignment is highly deformation-dependent.

The fitting of network behavior to a series of different deformations is shown in Fig. 5. We see that under relatively large strains, the W^f vs. λ^f curves become more similar. At small to moderate strains, the non-affinity of the deformation can play a significant role in the mechanics of the network, causing the plot of W^f vs. λ^f to become strongly deformation-dependent (Fig. 5b). In the case of Fig. 5, for example, a single HGO model cannot match the network model for all possible deformations, or even for specific families of deformations.

3.2 Alignment Dependence for Delaunay Networks

A total of 750 networks with different orientations ranging from isotropic ($H_{11} = 0.33$) to strongly aligned ($H_{11} = 0.8$) were studied, with the five representative networks (numbers 1–5) examined in detail in Fig. 6. The network views in Fig. 6a (xy-view) and Fig. 6b (xz-view) show markedly different alignments. The orientations of these networks start with network 1 being nearly isotropic, network 2 being slightly aligned in the x-direction, network 3 being slightly aligned in the z-direction, network 4 being more strongly aligned in the x-direction, and network 5 being even more strongly aligned in the x-direction, as demonstrated by the numbering in Fig. 6d–f. The W^f vs. λ^f curves were plotted for each network, and an HGO curve was fit to them (Fig. 6c). It is evident from these W^f vs. λ^f plots that the fit of the HGO model becomes more variable for more highly aligned fiber networks, especially at large strains. Another particularly interesting aspect of these plots is the behavior of network 3. The W^f vs. λ^f plot would indicate that the direction transverse to the alignment direction is actually stiffer than that in the direction of alignment. However, this is not the whole story. The fiber stretch values are the double contraction of

the orientation tensor and the right Cauchy-Green tensor, so when stretching in directions transverse to the primary alignment, much greater magnitudes of stretch are necessary to produce the same averaged fiber family stretch. In fact, the magnitude of the xy-biaxial stretch in network 3 was 3.33, while the magnitude of the xz-biaxial stretch was only 1.17. This effect is further evidence of the non-affine fiber realignment occurring in fiber networks that is not well captured by the HGO model. Fig. 6c also shows that the deformations corresponding with alignment are similar to what was observed in Fig. 5. For network 1, all deformations form a tight cluster of W^f vs. λ^f curves because the fibers are nearly isotropic. Network 2 shows slightly more spread since the primary orientation is more strongly aligned in the x-direction, and networks 4 and 5 exhibit even greater spread due to increased alignment in the primary x-direction.

Despite the differing W^f vs. λ^f behavior with different deformations, we still require an initial set of parameters for our simulations. We therefore fit a pair of model parameters C_2 and C_3 from Eq. 2 to the W^f vs. λ^f curves to allow us to readily determine material parameters without the need to run any additional simulations. We observed that the fitted parameters C_2 and C_3 were not constant over all networks, but showed considerable variation with network alignment. This result indicates that the degree of non-affinity, as indicated by the amount of correction necessary to convert the discrete fiber network model into an affine model, is dependent on fiber alignment. This result was previously obtained by Hatami-Marbini and Picu [37], who found a greater degree of non-affinity in aligned networks loaded transverse to the preferred direction of alignment. The importance of this result lies in the fact that the constants C_2 and C_3 depend the fiber network orientation, *even for networks constructed of identical fibers and even when orientation is included in the continuum model via the construct* $H_{IJ}C_{IJ}$.

To further explore the observed dependence, contour graphs of the calculated parameters, C_2 and C_3, were generated as a function of the alignment in the 1 and 2 directions (H_{11} and H_{22}, respectively) for all networks simulated (Fig. 6d and 6e). The location of networks of Fig. 6a and 6b are indicated on the contours with numbers 1–5. The non-smooth appearance of the contour lines must derive from other factors that contribute to the network behavior. However, H_{11} and H_{22} are sufficient to capture the general trend via the quadratic curve fits shown in Fig. 6f and 6g. The equations for those fits,

$$C_2 = \sum_{i=0}^{2} \sum_{j=0}^{2} \alpha_{ij} H_{11}^i H_{22}^j \qquad \text{Eq. 11A}$$

$$C_3 = \sum_{i=0}^{2} \sum_{j=0}^{2} \beta_{ij} H_{11}^i H_{22}^j \qquad \text{Eq. 11B}$$

allow estimation of C_2 and C_3 for any Delaunay network of fibers with the underlying properties specified above (Eq. 6). The goodness of fit was marginal ($R^2 = 0.47$ for C_2 and $R2 = 0.73$ for C_3) due to the inherent differences between networks and other factors influencing behavior (i.e. even networks with the same alignment have varied nodal positions and fiber lengths, which can change the network response to stretch). The coefficient values are given in Table 1.

Large values of C_2 and the smallest values of C_3 occur when the network is close to isotropic (point 1 in Fig. 6d and 6e). *If one desires to represent the behavior of an isotropic, non-affinely deforming discrete-fiber network with an affine-deformation model, the underlying fiber model in the network needs to be stiffer and less nonlinear compared to that representing a more strongly aligned network (point 5 in Fig. 6d and 6e).* As a simple verification, suppose we have the network shown in Fig. 7a having $H_{IJ} = \begin{bmatrix} 2/3 & 0 \\ 0 & 1/3 \end{bmatrix}$. If we stretch in the direction of fibers as shown in Fig. 7b where $F_{iJ} = \begin{bmatrix} 3/2 & 0 \\ 0 & 2/3 \end{bmatrix}$ and $C_{IJ} = \begin{bmatrix} 9/4 & 0 \\ 0 & 4/9 \end{bmatrix}$, we have an estimated average fiber stretch of $\langle \lambda_f \rangle = \sqrt{H_{IJ}C_{IJ}} = \sqrt{3/2 + 4/27} = 1.284$. If we simply compute the average stretch of the three fibers we have $\lambda_1 = 2/3$ and $\lambda_2 = \lambda_3 = 3/2$ which gives us a mean stretch of $\bar{\lambda} = 1.222$. Now if we take the same network and stretch transverse to the direction of alignment as shown in Fig. 7c where $F_{iJ} = \begin{bmatrix} 2/3 & 0 \\ 0 & 3/2 \end{bmatrix}$ and $C_{IJ} = \begin{bmatrix} 4/9 & 0 \\ 0 & 9/4 \end{bmatrix}$, we get an estimated average stretch of $\langle \lambda_f \rangle = \sqrt{8/27 + 3/4} = 1.023$. If we then compute the actual stretches by computing the equilibrium positions assuming that the fiber forces are linear in strain such that sum of vertical forces is zero:

$$\sum f_y = 0 = (L_1/l - 1) - 2(L_2/l - 1)\cos(\theta) \quad \text{Eq. 12}$$

and enforcing the geometric constraints that $L_2 \cos(\theta) + L_1 = 1.5/2$ and $2L_2 \sin(\theta) = 1/1.5$, we can solve giving $L_1 = 0.439$, $L_2 = 0.456$, and $\theta = 47.0°$. Thus, the stretches are $\lambda_1 = 0.88$ and $\lambda_2 = \lambda_3 = 0.91$ giving an average stretch of $\bar{\lambda} = 0.900$. This example leads us to two observations: 1. The estimated stretch transverse to the direction of alignment is far from that in the direction of alignment, and 2. The estimated behavior of the stretch transverse to the direction of alignment is not representative of the true average, and is, in fact, indicating the network is in tension when the true behavior of the network shows all the fibers in compression. This simple example drives home the point that the networks estimated using the structure tensor, H_{IJ} can be quite different from the real network behavior when the network is loaded transverse to its preferred direction of alignment. In this case, the network itself is very non-affine and should require a larger correction which is observed in Fig. 6d–e. Further, this result demonstrates the issue one can encounter when trying to fit the network behavior to the HGO model where the network itself develops almost no stress (effectively zero since the fibers buckle in compression) despite the fact that the HGO model using the structure tensor and calculating $\langle I_4 \rangle$ indicates the fibers should be in tension. This results in a fitted HGO fiber stiffness of ~0, which is clearly unphysical in general, but may be true for certain deformations. This effect is one that we must account for in our fitting method as discussed in Section 2.5 above.

3.3 Case Study: Single-Network Model Performance for Non-Fitted Deformation

A simple validation of the initial HGO fit and refit process is shown in Fig. 8. The initial HGO fit of uniaxial, biaxial, and shear deformations produces stresses of a similar magnitude as the network simulation under the deformation given in Eq. 9 (Fig. 8a). However, the results show large discrepancies in the shape of the curve (Fig. 8a), which

are largely corrected in the refit process (Fig. 8b). The study presented indicates the viability of fitting an HGO model using the underlying orientation and a generated W^f vs. λ^f for many deformations to give a rough estimate of parameters, while highlighting importance of the refit process to producing the proper behavior. Further, this case study demonstrates how network mechanics vary significantly from the extrapolated HGO model under different deformations.

3.4 Comparison to Full Multiscale Simulations

Maximum shear stress and strain fields are shown for the multiscale model, initial HGO model, and refit HGO model (Fig. 9). The maximum shear stress and strain distribution of the HGO model compared to the multiscale model are visually similar, and the HGO model was able to predict the regions of high shear stress and strain. The initial HGO model parameters underpredicted the magnitude of the maximum shear stress and overpredicted the max shear strains in these regions, but the accuracy of the tissue's stress prediction improved with a refit of the HGO parameters with each element's average deformation gradient tensor. The refit HGO model more accurately localized regions of high tissue shear stress, at the cost of a small increase in the tissue's strain, when compared to the initial HGO model. This observation is supported by the improvement of RMS error of the refit HGO model maximum shear stress compared to the initial HGO model. The RMS errors for the initial HGO model maximum shear stress and strain are 0.074 MPa, and 3.28%, respectively. The RMS errors for the refit HGO model maximum shear stress and strain are 0.062 MPa, and 4.12%, respectively. Further, the computation time for the entire HGO simulation including the final step refit is shown in Table 2. The time to run the HGO simulation is orders of magnitude decreased over the full multiscale simulation.

4. Discussion

4.1 Major Findings and Potential Significance

In this work, we developed a hybrid microstructural-continuum multiscale model to reproduce the macroscopic constitutive behavior of a structure-based multiscale simulation. This paper presents methods to speed up the model construction and full analysis of a discrete-fiber multiscale model while accounting for the microstructural details of a heterogeneous tissue such as FCL. The proposed work uses the structural parameters of discrete fiber networks in a continuous-fiber model such as HGO to decrease the computational cost of a full multiscale simulation of a heterogeneous tissue from 2622.69 to 1.48 CPU-hours as is shown in Table 2.

We found that the macroscopic-scale behavior of a Delaunay network can be reasonably described using the HGO model, but the accuracy of the approximation is dependent on the degree of alignment of the fiber network, the type of deformation imposed, and the magnitude of the deformation. The results of Fig. 5 and Fig. 6c indicate that simulations within a certain family of deformation types (uniaxial, biaxial, shear) can be fit with a high degree of confidence. The results of Fig. 6c and Fig. 8 suggest that extrapolating beyond the fitting range can give an overall rough estimate of behavior, but it is important to update the parameters based on the deformation. If the deformation of interest is known

(e.g., one knows that the system will be loaded in equibiaxial extension), then one can simply fit a model to that deformation and use the model, but the deformation of interest is almost never known *a priori*. Even if the type of deformation or the boundary conditions are known, however, the magnitude of the deformation is often unknown, and tissue heterogeneity virtually assures that the local deformation is different from the applied (global) deformation, so it is essential to have a procedure that can be used to provide a good initial guess of the continuum model parameters one needs, as well as a method for updating the parameters. This work demonstrates reasonable methods for selection of initial parameters via fitting multiple deformations, and a refitting process based on the simulation deformation gradient.

In addition, we have described how stronger alignment of Delaunay networks results in more dissimilar behavior between deformations in terms of W^f vs. λ^f curves (Fig. 6c). This result, while not unexpected based on previous studies [37], is significant because it further emphasizes the importance of the refit process and the challenges of trying to use an affine model to describe a material that exhibits non-affine behavior. The networks also showed increased nonlinearity and fiber modulus with alignment, which further indicates that inherent non-affinity alters the apparent mechanical response of the tissue. We further offered a simple verification of this result in the example in Fig. 7, which further demonstrates the pitfalls in assuming affine behavior in the modeling of fibrous tissues. Particularly, one must be cautious when one starts to probe local phenomena such as cell-ECM interactions or tissue failure in affine continuous models.

Taken together, these results indicate that the HGO model itself does not fully capture the change in network behavior with the generalized structure tensor, H_{IJ}. One issue with this structure tensor is that, to properly capture the behavior of a dispersed fiber population with a tension-compression switch, one needs to recalculate the tensor using only the tensile fibers. In an ideal case, this would be done for each deformation step (alternative approaches are not given here, but are discussed in [34, 64]). Such an approach could help alleviate some of these differences observed in the current study, but the cost of performing a spherical integration over 3D distributions of fibers might well prove greater than that of the simple refit process, especially for multiple fiber families or multiple fiber types. Some network models, might be better fit, to a certain extent, by a compressed-fiber-excluding macroscopic model, and a more thorough testing regimen achievable via computational vs. experimental tests may provide more insight into exactly what behaviors are captured or lost by such models. Future in-depth studies of on the translation of a discrete, fiber-level tension-compression switch to a macroscopic fiber compression exclusion model are merited.

As discussed above, we do not account for the fiber tension-compression asymmetry in the calculation of H_{IJ}. That is, H_{IJ} is calculated based on all fibers in the initial state. We instead capture the fiber tension-compression switch through the fiber constitutive law, which is much stiffer in tension than in compression. The tension-compression switch of fibers is intrinsic to the microstructural model, so we remove the requirement for fiber exclusion from the structure tensor [5, 64]. The HGO parameters C2 and C3, which are fit to the results of the microstructural simulations, are thus informed by the tension-compression

asymmetry inherent to the model. It may be possible that a better fit of the microstructural model could be obtained by an HGO model with a tension-compression switch, but that possibility was not explored in the current work.

We further described how a curve-fit of multiple simulations could allow one to select continuous model parameters to represent Delaunay networks with arbitrary orientation without rerunning simulations (Fig. 6). The construction of such databases of properties for networks can further simplify the assessment of material parameters that describe network behavior. While the equations show a high degree of variance, construction of a broad curve-fit of parameter values can give us a reasonable starting point for a wide range of networks. The initial fitting of the network behavior to multiple deformations is the largest contribution to the overall time spent on simulation for the HGO FE model (Table 2). Thus, if one can select starting parameters based on network orientation and some other metric of network construction like network type (Delaunay, Voronoi, etc.), one can greatly reduce the time to produce simulations. In fact, this method of reproducing network parameters from pre-defined relations rather than having to generate and run the networks could have a significant impact on creation and simulation of multiscale tissue models, allowing for many hypotheses to be tested quickly with regards to fiber orientations, tissue composition, or localized defects. If such a strategy is to be pursued, however, it is imperative that the starting parameter values be based on networks similar to the ones being used in the simulation.

We describe the application of the microstructural-to-HGO modelling strategy to a finite-element simulation. This simulation shows similar results to a full multiscale simulation (Fig. 9) while reducing the model construction and simulation time by orders of magnitude over a full multiscale approach (Table 2). As mentioned previously, this approach, combined with estimation of material parameters without generating and simulating networks, could enable multiscale simulations without the need for a supercomputing cluster. Eliminating the necessity of bridging micro- to mm-scale could also open up opportunities to take tissue multiscale approaches up another scale level to organ or full-body kinematics, further helping us identify things like the role local FCL defects play in the spine or elucidating the role of microstructure in aneurysm mechanics.

4.2 Model Limitations

As with all models, the proposed system has several limitations. First, because the HGO model is an imperfect estimator of actual network behavior, there will be intrinsic errors even after the proposed refitting procedure. One could perform this analysis with other constitutive models that may capture specific behavior differently as compared to the HGO model (take for example the Blatz-Ko material for compressible materials like collagen gels [77], or any of a number of actively contracting models for vascular tissues such as [78–80]). The proposed technique is adaptable to different constitutive models, and could be fit to multiple affine models to select the best choice.

As noted above, the HGO model did not fully capture the observed network behavior. We observe that a strength of our approach is that the computational experiments are not limited by the physical realities of equipment design and sample damage, so one can perform

any experiment desired and as many experiments as desired. As a result, any inability of the continuum-scale model to capture the micro-scale network model's behavior will be apparent. Whether this effect is a positive or negative feature depends on the perspective of the user: it virtually guarantees inconsistency between the micro- and macro-scale models in some deformation, but it enables the user to see exactly where and how severe such inconsistency is, which could be valuable. For example, one could decide that the inaccuracy is in a range of deformations that are not physiologically relevant, or the inconsistency could inspire the development of new constitutive models at the continuum scale.

Another limitation of the approach in current form is the restriction to a single, non-evolving network. A major advantage of the full multiscale approach is the ability to accommodate changes in the network due to, e.g., failure [38, 58, 81] or remodeling [59, 82]. In the case of an evolving network, the macroscale parameters would necessarily have to be refit at each step. Knowing the deformation state at the previous step could allow for efficient re-fitting, but there is much work still to be done to identify the optimal strategy for such problems. Similarly, in particular in the case of the arterial wall, multicomponent models are important at both the microstructural [38, 58, 60] and macrostructural [83–86] scales, and the best strategy to fit a multicomponent, discrete-fiber microstructural model is by no means clear and has not been explored in this work.

Lastly, compressing the network in the direction in which most fibers are aligned might result in average of fiber stretch ($\hat{\lambda}_f$) less than one. In this case, some fibers are still stretched leading to a rise in the strain energy. The fitting procedure will be unable to capture these behaviors, and such artifacts will cause an increase in the stiffness of the model, since the slope of W^f vs. λ^f curve, i.e. stress, will be artificially increased as the fit attempts to match the network when average stretch becomes greater than one (i.e. W_f has been increasing from the network model since some fibers are in tension, but the overall average $\hat{\lambda}_f$ is still less than one, thus the fit must be stiffer than the network in order to minimize the distance between the curves). Conversely, as observed in the example given in Fig. 7, it is also possible for the average fiber stretch $\hat{\lambda}_f$ to give a value greater than one, while the true average is less than one. This would indicate that the fibers themselves have a negligible effect on the behavior. While this might be true for a specific deformation, it is, in general, not an accurate representation of the material, and thus requires special care to be taken in the fitting process. These problems are mostly theoretical, since tissues are almost always loaded in the direction that their fibers are aligned, but it is nonetheless important to make sure there is a method for dealing with this issue in this framework. We offer one solution in this work, but it is by no means the only way to deal with this issue.

5. Conclusions

In this work, we have demonstrated a novel technique for simulating multiscale biological tissues. This work focuses on simple microstructures applied to complex finite element geometries, but this technique can be expanded for any microstructural model. The present method gives us flexibility to perform large-scale simulations while maintaining microstructural detail.

Acknowledgments

In this special issue in honor of Gerhard Holzapfel's remarkable contributions to the field of tissue mechanics, the authors are happy to express their gratitude for his hard work, devotion to high-quality science, and commitment to the biomechanics community. He is both a great scientist and a great person, and we are lucky to have him as a colleague.

Funding

This work was supported by the National Institutes of Health through the grants U01 AT010326, U54 CA210190, T32 AR050938, and U01 HL139471. Ryan R. Mahutga and Lauren M. Bersie-Larson are supported by University of Minnesota Doctoral Dissertation Fellowships. Ryan R. Mahutga was supported by National Science Foundation Graduate Research Fellowship Program (NSF GRFP) under Grant No. 00039202. Any opinion, findings, and conclusions or recommendations expressed in this material are those of the authors(s) and do not necessarily reflect the views of the National Science Foundation.

References

1. Holzapfel GA, Gasser TC, Ogden RW: A new constitutive framework for arterial wall mechanics and a comparative study of material models. J. Elast. 61, 1–48 (2000). 10.1023/A:1010835316564
2. Gasser TC, Ogden RW, Holzapfel GA: Hyperelastic modelling of arterial layers with distributed collagen fibre orientations. 10.1098/rsif.2005.0073
3. Holzapfel GA: Biomechanics of Soft Tissue. In: The Handbook of Materials Behavior Models pp. 1049–1063. Academic Press (2001)
4. Humphrey JD: Cardiovascular Solid Mechanics. (2002)
5. Volokh KY: On arterial fiber dispersion and auxetic effect. J. Biomech. 61, 123–130 (2017). 10.1016/j.jbiomech.2017.07.010 [PubMed: 28774466]
6. Gatt R, Vella Wood M, Gatt A, Zarb F, Formosa C, Azzopardi KM, Casha A, Agius TP, Schembri-Wismayer P, Attard L, Chockalingam N, Grima JN: Negative Poisson's ratios in tendons: An unexpected mechanical response. Acta Biomater. 24, 201–208 (2015). 10.1016/J.ACTBIO.2015.06.018 [PubMed: 26102335]
7. Nolan DR, Mcgarry JP: On the Compressibility of Arterial Tissue. Ann. Biomed. Eng. 44,. 10.1007/s10439-015-1417-1
8. Puccio, Di F, Celi S, Forte P: Review of Experimental Investigations on Compressibility of Arteries and Introduction of a New Apparatus. 10.1007/s11340-012-9614-4
9. Yosibash Z, Manor I, Gilad I, Willentz U: Experimental evidence of the compressibility of arteries. J. Mech. Behav. Biomed. Mater. 39, 339–354 (2014). 10.1016/J.JMBBM.2014.07.030 [PubMed: 25173235]
10. Yossef OE, Farajian M, Gilad I, Willenz U, Gutman N, Yosibash Z: Further experimental evidence of the compressibility of arteries. J. Mech. Behav. Biomed. Mater. 65, 177–189 (2017). 10.1016/J.JMBBM.2016.08.013 [PubMed: 27578431]
11. Guo X, Kassab GS: Variation of mechanical properties along the length of the aorta in C57bl/6 mice. Am. J. Physiol. Circ. Physiol (2003). 10.1152/ajpheart.00567.2003
12. Fung YC: Elasticity of soft tissues in simple elongation. Am. J. Physiol. 213, 1532–1544 (1967). 10.1152/ajplegacy.1967.213.6.1532 [PubMed: 6075755]
13. Bellini C, Ferruzzi J, Roccabianca S, Di Martino ES, Humphrey JD: A Microstructurally Motivated Model of Arterial Wall Mechanics with Mechanobiological Implications. 10.1007/s10439-013-0928-x
14. Holzapfel GA, Ogden RW: An Arterial Constitutive Model Accounting for Collagen Content and Cross-Linking. J. Mech. Phys. Solids. 103682 (2019). 10.1016/J.JMPS.2019.103682
15. Li K, Ogden RW, Holzapfel GA: An exponential constitutive model excluding fibres under compression: Application to extension–inflation of a residually stressed carotid artery. Math. Mech. Solids. 23, 1206–1224 (2018). 10.1177/1081286517712077
16. Cheng JK, Stoilov I, Mecham RP, Wagenseil JE: A fiber-based constitutive model predicts changes in amount and organization of matrix proteins with development and disease in the mouse aorta. Biomech. Model. Mechanobiol. (2013). 10.1007/s10237-012-0420-9

17. Gasser TC, Schulze-Bauer CAJ, Holzapfel GA: A three-dimensional finite element model for arterial clamping. J. Biomech. Eng. 124, 355–363 (2002). 10.1115/1.1485284 [PubMed: 12188202]
18. Mihai LA, Budday S, Holzapfel GA, Kuhl E, Goriely A: A family of hyperelastic models for human brain tissue. J. Mech. Phys. Solids. 106, 60–79 (2017). 10.1016/j.jmps.2017.05.015
19. Claeson AAAA, Barocas VHVH: Planar biaxial extension of the lumbar facet capsular ligament reveals significant in-plane shear forces. J. Mech. Behav. Biomed. Mater. 65, 127–136 (2017). 10.1016/j.jmbbm.2016.08.019 [PubMed: 27569760]
20. Guan D, Ahmad F, Theobald P, Soe S, Luo X, Gao H: On the AIC-based model reduction for the general Holzapfel–Ogden myocardial constitutive law. Biomech. Model. Mechanobiol. 18, 1213–1232 (2019). 10.1007/s10237-019-01140-6 [PubMed: 30945052]
21. Holzapfel GA, Ogden RW: Constitutive modelling of passive myocardium: a structurally based framework for material characterization. Trans. R. Soc. A. 367, 3445–3475 (2009). 10.1098/rsta.2009.0091
22. Laurence DW, Johnson EL, Hsu M, Baumwart R, Mir A, Burkhart HM, Holzapfel GA, Wu Y, Lee C: A pilot in silico modelling-based study of the pathological effects on the biomechanical function of tricuspid valves. Int. j. numer. method. biomed. eng. 36, (2020). 10.1002/cnm.3346
23. Shahraki NM, Fatemi A, Goel VK, Agarwal A: On the use of biaxial properties in modeling annulus as a Holzapfel-Gasser-Ogden material. Front. Bioeng. Biotechnol. 3, 69 (2015). 10.3389/fbioe.2015.00069 [PubMed: 26090359]
24. Gasser TC, Holzapfel GA: Modeling plaque fissuring and dissection during balloon angioplasty intervention. Ann. Biomed. Eng. 35, 711–723 (2007). 10.1007/s10439-007-9258-1 [PubMed: 17385047]
25. McEvoy E, Holzapfel GA, McGarry P: Compressibility and Anisotropy of the Ventricular Myocardium: Experimental Analysis and Microstructural Modeling. J. Biomech. Eng. 140, (2018). 10.1115/1.4039947
26. Khayyeri H, Longo G, Gustafsson A, Isaksson H: Comparison of structural anisotropic soft tissue models for simulating Achilles tendon tensile behaviour. J. Mech. Behav. Biomed. Mater. 61, 431–443 (2016). 10.1016/j.jmbbm.2016.04.007 [PubMed: 27108350]
27. Laville C, Pradille C, Tillier Y: Mechanical characterization and identification of material parameters of porcine aortic valve leaflets. J. Mech. Behav. Biomed. Mater. 112, 104036 (2020). 10.1016/j.jmbbm.2020.104036 [PubMed: 32882679]
28. Rodríguez JF, Ruiz C, Doblaré M, Holzapfel GA: Mechanical stresses in abdominal aortic aneurysms: Influence of diameter, asymmetry, and material anisotropy. J. Biomech. Eng. 130, (2008). 10.1115/1.2898830
29. Holzapfel GA, Niestrawska JA, Ogden RW, Reinisch AJ, Schriefl AJ: Modelling non-symmetric collagen fibre dispersion in arterial walls. 10.1098/rsif.2015.0188
30. Li K, Ogden RW, Holzapfel GA: A discrete fibre dispersion method for excluding fibres under compression in the modelling of fibrous tissues. J. R. Soc. Interface. 15, 20170766 (2018). 10.1098/rsif.2017.0766 [PubMed: 29386399]
31. Li K, Ogden RW, Holzapfel GA: Modeling fibrous biological tissues with a general invariant that excludes compressed fibers. J. Mech. Phys. Solids. 110, 38–53 (2018). 10.1016/j.jmps.2017.09.005
32. Nolan DR, Gower AL, Destrade M, Ogden RW, McGarry JP: A robust anisotropic hyperelastic formulation for the modelling of soft tissue. J. Mech. Behav. Biomed. Mater. 39, 48–60 (2014). 10.1016/j.jmbbm.2014.06.016 [PubMed: 25104546]
33. Latorre M, Montáns FJ: On the tension-compression switch of the Gasser-Ogden-Holzapfel model: Analysis and a new pre-integrated proposal. J. Mech. Behav. Biomed. Mater. 57, 175–189 (2016). 10.1016/j.jmbbm.2015.11.018 [PubMed: 26720909]
34. Melnik AV, Borja Da Rocha H, Goriely A: On the modeling of fiber dispersion in fiber-reinforced elastic materials. Int. J. Non. Linear. Mech. 75, 92–106 (2015). 10.1016/j.ijnonlinmec.2014.10.006
35. Lanir Y: Constitutive equations for fibrous connective tissues. J. Biomech. 18, 1 (1983)

36. Chandran PL, Barocas VH: Affine Versus Non-Affine Fibril Kinematics in Collagen Networks: Theoretical Studies of Network Behavior. J. Biomech. Eng. 128, 259–270 (2006). 10.1115/1.2165699 [PubMed: 16524339]
37. Hatami-Marbini H, Picu RC: Effect of fiber orientation on the non-affine deformation of random fiber networks. Acta Mech. 205, 77–84 (2009). 10.1007/s00707-009-0170-7
38. Korenczuk CE, Dhume RY, Liao K, Barocas VH: Ex Vivo Mechanical Tests and Multiscale Computational Modeling Highlight the Importance of Intramural Shear Stress in Ascending Thoracic Aortic Aneurysms. J. Biomech. Eng. (2019). 10.1115/1.4045270
39. Zhang S, Zarei V, Winkelstein BA, Barocas VH: Multiscale mechanics of the cervical facet capsular ligament, with particular emphasis on anomalous fiber realignment prior to tissue failure. Biomech. Model. Mechanobiol. 17, 133–145 (2018). 10.1007/s10237-017-0949-8 [PubMed: 28821971]
40. Marino M, Vairo G: Stress and strain localization in stretched collagenous tissues via a multiscale modelling approach. Comput. Methods Biomech. Biomed. Engin. 17, 11–30 (2014). 10.1080/10255842.2012.658043 [PubMed: 22525051]
41. Weinberg EJ, Kaazempur Mofrad MR: A multiscale computational comparison of the bicuspid and tricuspid aortic valves in relation to calcific aortic stenosis. J. Biomech. 41, 3482–3487 (2008). 10.1016/j.jbiomech.2008.08.006 [PubMed: 18996528]
42. Weinberg EJ, Mofrad MRK: Three-dimensional, multiscale simulations of the human aortic valve. Cardiovasc. Eng. 7, 140–155 (2007). 10.1007/s10558-007-9038-4 [PubMed: 18026835]
43. Zarei V, Liu CJ, Claeson AA, Akkin T, Barocas VH: Image-based multiscale mechanical modeling shows the importance of structural heterogeneity in the human lumbar facet capsular ligament. Biomech. Model. Mechanobiol. 16, 1425–1438 (2017). 10.1007/s10237-017-0896-4 [PubMed: 28361294]
44. Barocas VH: Multiscale, Structure-Based Modeling for the Elastic Mechanical Behavior of Arterial Walls. J. Biomech. Eng. 129, 611 (2007). 10.1115/1.2746387 [PubMed: 17655483]
45. Sander E, Stylianopoulos T, Tranquillo R, Barocas V: Image-based biomechanics of collagen-based tissue equivalents. IEEE Eng. Med. Biol. Mag. 28, 10–18 (2009). 10.1109/MEMB.2009.932486
46. Gonc -Alves Coelho P, Fernandes PR, Carric -O Rodrigues H: Multiscale modeling of bone tissue with surface and permeability control. 10.1016/j.jbiomech.2010.10.007
47. Virgilio KM, Martin KS, Peirce SM, Blemker SS: Multiscale models of skeletal muscle reveal the complex effects of muscular dystrophy on tissue mechanics and damage susceptibility. Interface Focus. 5, 20140080 (2015). 10.1098/rsfs.2014.0080 [PubMed: 25844152]
48. Korenczuk CE, Barocas VH, Richardson WJ: Effects of Collagen Heterogeneity on Myocardial Infarct Mechanics in a Multiscale Fiber Network Model. J. Biomech. Eng. 141, (2019). 10.1115/1.4043865
49. Maceri F, Marino M, Vairo G: A unified multiscale mechanical model for soft collagenous tissues with regular fiber arrangement. J. Biomech. 43, 355–363 (2010). 10.1016/j.jbiomech.2009.07.040 [PubMed: 19837410]
50. Hatami-Marbini H, Shahsavari A, Picu RC: Multiscale modeling of semiflexible random fibrous structures. CAD Comput. Aided Des. 45, 77–83 (2013). 10.1016/j.cad.2011.10.002
51. Gasser TC, Holzapfel GA: Modeling the propagation of arterial dissection. Eur. J. Mech. A/Solids. 25, 617–633 (2006). 10.1016/j.euromechsol.2006.05.004
52. Horvat N, Virag L, Holzapfel GA, Sorić J, Karšaj I: A finite element implementation of a growth and remodeling model for soft biological tissues: Verification and application to abdominal aortic aneurysms. Comput. Methods Appl. Mech. Eng. 352, 586–605 (2019). 10.1016/j.cma.2019.04.041
53. Fereidoonnezhad B, Naghdabadi R, Sohrabpour S, Holzapfel GA: A Mechanobiological model for damage-induced growth in arterial tissue with application to in-stent restenosis. J. Mech. Phys. Solids. 101, 311–327 (2017). 10.1016/j.jmps.2017.01.016
54. Rolf-Pissarczyk M, Li K, Fleischmann D, Holzapfel GA: A discrete approach for modeling degraded elastic fibers in aortic dissection. Comput. Methods Appl. Mech. Eng. 373, 113511 (2021). 10.1016/j.cma.2020.113511

55. Mao W, Caballero A, McKay R, Primiano C, Sun W: Fully-coupled fluid-structure interaction simulation of the aortic and mitral valves in a realistic 3D left ventricle model. PLoS One. 12, e0184729 (2017). 10.1371/journal.pone.0184729 [PubMed: 28886196]
56. Balzani D, Brinkhues S, Holzapfel GA: Constitutive framework for the modeling of damage in collagenous soft tissues with application to arterial walls. Comput. Methods Appl. Mech. Eng. 213–216, 139–151 (2012). 10.1016/j.cma.2011.11.015
57. Erdemir A, Bennetts C, Davis S, Reddy A, Sibole S: Multiscale cartilage biomechanics: technical challenges in realizing a high-throughput modelling and simulation workflow. Interface Focus. 5, 20140081 (2015). 10.1098/rsfs.2014.0081 [PubMed: 25844153]
58. Witzenburg CMCM, Dhume RYRY, Shah SBSB, Korenczuk CECE, Wagner HPHP, Alford PWPW, Barocas VHVH: Failure of the Porcine Ascending Aorta: Multidirectional Experiments and a Unifying Microstructural Model. J. Biomech. Eng. 139, 031005 (2017). 10.1115/1.4035264
59. Bersie-Larson LM, Gyoneva L, Goodman DJ, Dorfman KD, Segal Y, Barocas VH: Glomerular filtration and podocyte tensional homeostasis: importance of the minor type IV collagen network. Biomech. Model. Mechanobiol. (2020). 10.1007/s10237-020-01347-y
60. Mahutga RR, Barocas VH: Investigation of Pathophysiological Aspects of Aortic Growth, Remodeling, and Failure Using a Discrete-Fiber Microstructural Model. J. Biomech. Eng. 142, 111007 (2020). 10.1115/1.4048031 [PubMed: 32766738]
61. Sajjadinia SS, Carpentieri B, Holzapfel GA: A backward pre-stressing algorithm for efficient finite element implementation of in vivo material and geometrical parameters into fibril-reinforced mixture models of articular cartilage. J. Mech. Behav. Biomed. Mater. 104203 (2020). 10.1016/j.jmbbm.2020.104203 [PubMed: 33234496]
62. Gültekin O, Dal H, Holzapfel GA: Numerical aspects of anisotropic failure in soft biological tissues favor energy-based criteria: A rate-dependent anisotropic crack phase-field model. Comput. Methods Appl. Mech. Eng. 331, 23–52 (2018). 10.1016/j.cma.2017.11.008 [PubMed: 31649410]
63. Holzapfel GA, Stadler M, Gasser TC: Changes in the mechanical environment of stenotic arteries during interaction with stents: Computational assessment of parametric stent designs. J. Biomech. Eng. 127, 166–180 (2005). 10.1115/1.1835362 [PubMed: 15868799]
64. Holzapfel GA, Ogden RW, Sherifova S: On fibre dispersion modelling of soft biological tissues: A review, (2019)
65. Federico S, Gasser TC: Nonlinear elasticity of biological tissues with statistical fibre orientation. J. R. Soc. Interface. 7, (2010). 10.1098/rsif.2009.0502
66. Chandran PLPL, Barocas VHVH: Deterministic material-based averaging theory model of collagen gel micromechanics. J. Biomech. Eng. 129, 137 (2007). 10.1115/1.2472369 [PubMed: 17408318]
67. Little JS, Khalsa PS: Material Properties of the Human Lumbar Facet Joint Capsule. J. Biomech. Eng. 127, 15–24 (2005). 10.1115/1.1835348 [PubMed: 15868784]
68. Stender CJ, Rust E, Martin PT, Neumann EE, Brown RJ, Lujan TJ: Modeling the effect of collagen fibril alignment on ligament mechanical behavior. Biomech. Model. Mechanobiol. 17, 543–557 (2018). 10.1007/s10237-017-0977-4 [PubMed: 29177933]
69. Dhume RY, Shih ED, Barocas VH: Multiscale model of fatigue of collagen gels. Biomech. Model. Mechanobiol. 18, 175–187 (2019). 10.1007/s10237-018-1075-y [PubMed: 30151813]
70. Dhume RY, Barocas VH: Emergent structure-dependent relaxation spectra in viscoelastic fiber networks in extension. Acta Biomater. 87, 245–255 (2019). 10.1016/j.actbio.2019.01.027 [PubMed: 30682422]
71. Billiar KL, Sacks MS: Biaxial mechanical properties of the native and glutaraldehyde-treated aortic valve cusp: Part II - A structural constitutive model. J. Biomech. Eng. Asme. 122, 327–335 (2000)
72. Gacek E, Bermel EA, Ellingson AM, Barocas VH: Through-thickness Regional Variation in the Mechanical Characteristics of the Lumbar Facet Capsular Ligament. Biomech. Model. Mechanobiol. In Review, (2020)
73. Zarei V, Dhume RY, Ellingson AM, Barocas VH: Multiscale modelling of the human lumbar facet capsular ligament: analysing spinal motion from the joint to the neurons. J. R. Soc. Interface. 15, 20180550 (2018). 10.1098/rsif.2018.0550 [PubMed: 30429262]

74. Bermel EA, Barocas VH, Ellingson AM: The role of the facet capsular ligament in providing spinal stability. Comput. Methods Biomech. Biomed. Engin. 21, 712–721 (2018). 10.1080/10255842.2018.1514392 [PubMed: 30719929]

75. Maas SA, Ellis BJ, Ateshian GA, Weiss JA: FEBio: Finite elements for biomechanics. J. Biomech. Eng. 134, (2012). 10.1115/1.4005694

76. Maas SA, Rawlins D, Weiss JA, Ateshian GA: FEBio User Manual v2.8

77. Lane BA, Harmon KA, Goodwin RL, Yost MJ, Shazly T, Eberth JF: Constitutive modeling of compressible type-I collagen hydrogels. Med. Eng. Phys. 53, 39–48 (2018). 10.1016/j.medengphy.2018.01.003 [PubMed: 29396019]

78. Böl M, Reese S, Parker KK, Kuhl E: Computational modeling of muscular thin films for cardiac repair. Comput. Mech. 43, 535–544 (2009). 10.1007/s00466-008-0328-5

79. Eriksson T, Prassl A, Plank G, Holzapfel G: Influence of myocardial fiber/sheet orientations on left ventricular mechanical contraction. Math. Mech. Solids. 18, 592–606 (2013). 10.1177/1081286513485779

80. Win Z, Buksa JM, Alford PW: Architecture-Dependent Anisotropic Hysteresis in Smooth Muscle Cells. Biophys. J. 115, 2044–2054 (2018). 10.1016/j.bpj.2018.09.027 [PubMed: 30348447]

81. Vanderheiden SMSM, Hadi MFMF, Barocas VHVH: Crack Propagation Versus Fiber Alignment in Collagen Gels: Experiments and Multiscale Simulation. J. Biomech. Eng. 137, 121002 (2015). 10.1115/1.4031570 [PubMed: 26355475]

82. Hadi MFF, Sander EAA, Ruberti JWW, Barocas VHH: Simulated remodeling of loaded collagen networks via strain-dependent enzymatic degradation and constant-rate fiber growth. Mech. Mater. 44, 72–82 (2012). 10.1016/j.mechmat.2011.07.003 [PubMed: 22180691]

83. Zeinali-Davarani S, Wang Y, Chow MJ, Turcotte R, Zhang Y: Contribution of collagen fiber undulation to regional biomechanical properties along porcine thoracic aorta. J. Biomech. Eng. (2015). 10.1115/1.4029637

84. Smoljkić M, Fehervary H, Van den Bergh P, Jorge-Peñas A, Kluyskens L, Dymarkowski S, Verbrugghe P, Meuris B, Vander Sloten J, Famaey N: Biomechanical Characterization of Ascending Aortic Aneurysms. Biomech. Model. Mechanobiol. (2017). 10.1007/s10237-016-0848-4

85. Holzapfel GA, Ogden RW: Modelling the layer-specific three-dimensional residual stresses in arteries, with an application to the human aorta. J. R. Soc. Interface. 7, 787–799 (2010). 10.1098/rsif.2009.0357 [PubMed: 19828496]

86. Baek S, Valentin A, Humphrey JD: Biochemomechanics of cerebral vasospasm and its resolution: II. Constitutive relations and model simulations. Ann. Biomed. Eng. 35, 1498–1509 (2007). 10.1007/s10439-007-9322-x [PubMed: 17487585]

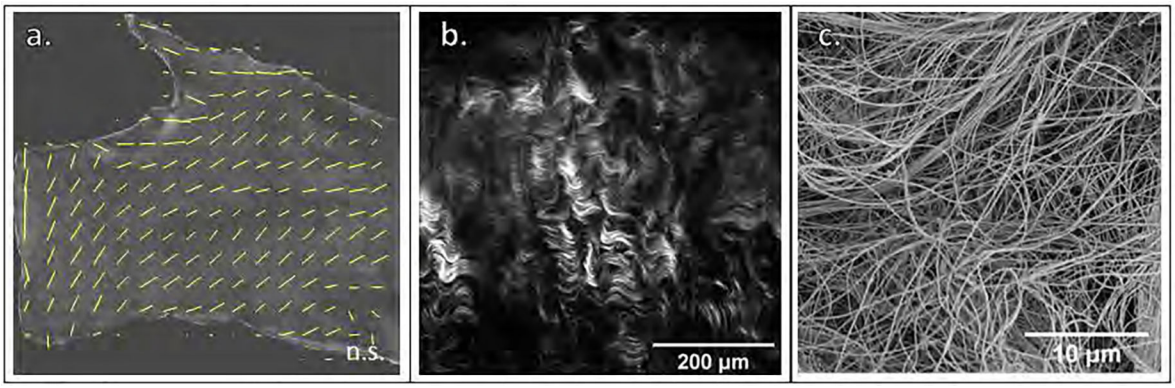

Fig. 1.

a. Quantitative Polarized Light Imaging (QPLI) of the brachiocephalic artery bifurcation showing macro-scale fiber orientation vectors. **b.** Second Harmonic Generation (SHG) imaging of collagen microstructure in the Facet Capsular Ligament (FCL). **c.** Scanning Electron Microscopy (SEM) of the collagen microstructure in the FCL

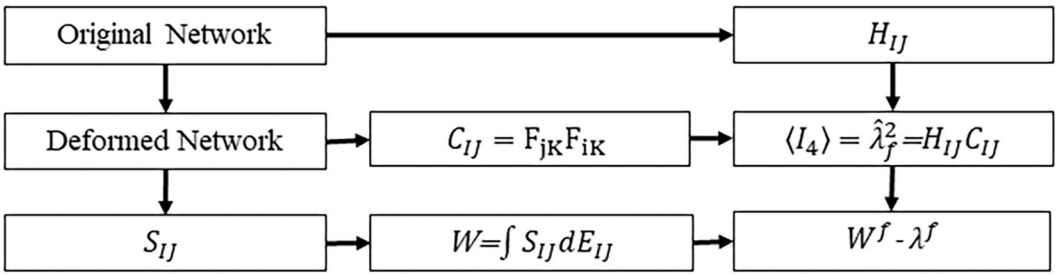

Fig. 2.
Flowchart for converting fiber network model to affine model

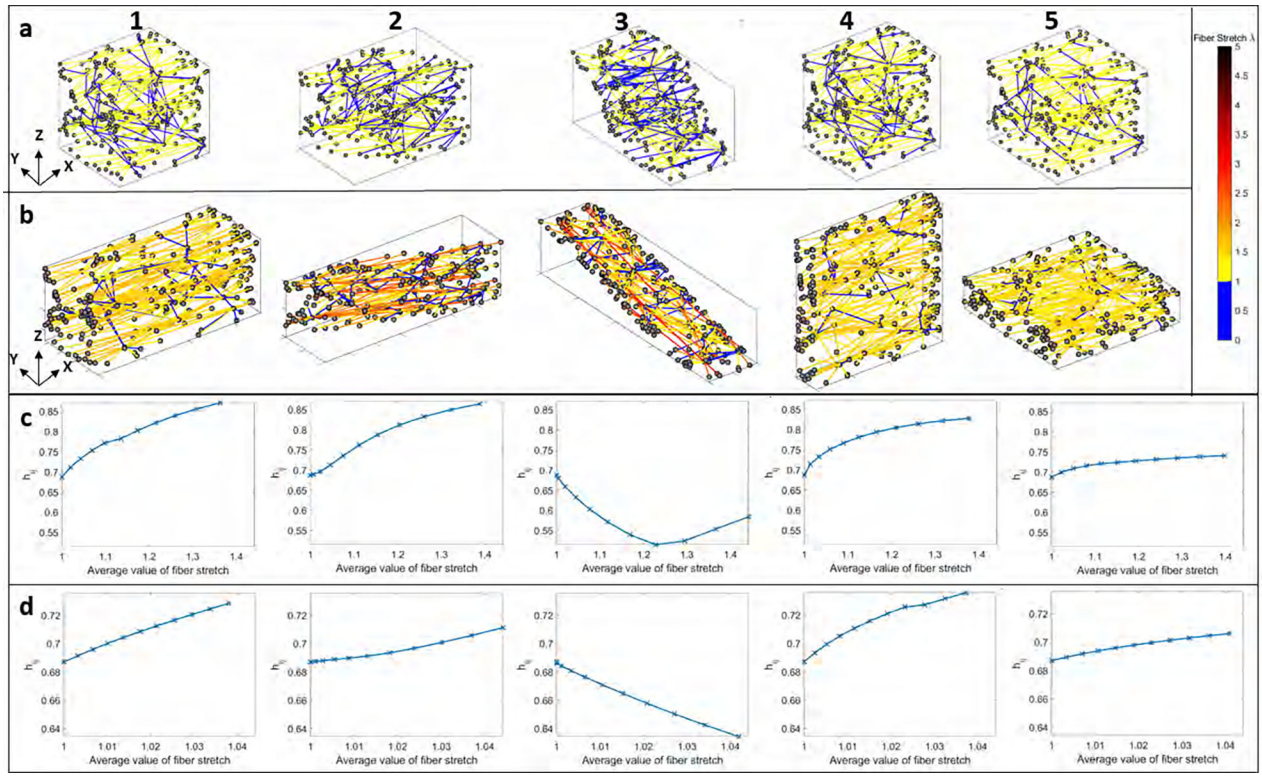

Fig. 3.

a1–5. Network deformations for x-uniaxial, xy-shear, yz-shear, xz-biaxial, xy-biaxial for 112% fiber Green strain. **b1–5.** Network deformations for x-uniaxial, xy-shear, yz-shear, xz-biaxial, xy-biaxial for 10% fiber Green strain. **c1–5.** The largest eigenvalue of the instantaneous orientation tensor, h_{ij} versus the average value of fiber stretch for 112% fiber Green strain. **d1–5.** The largest eigenvalue of the instantaneous orientation tensor, h_{ij} versus the average value of fiber stretch for 10% Green strain

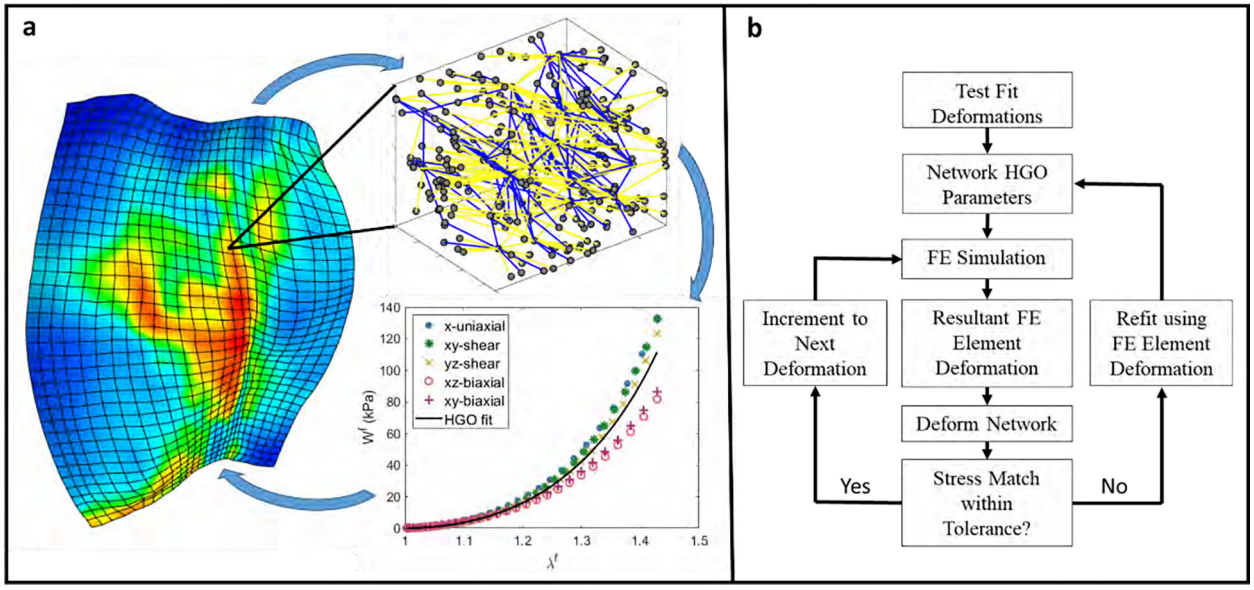

Fig. 4.

a. Schematic of the hybrid continuum-discrete multiscale approach. **b.** Flowchart for the hybrid continuum-discrete multiscale approach.

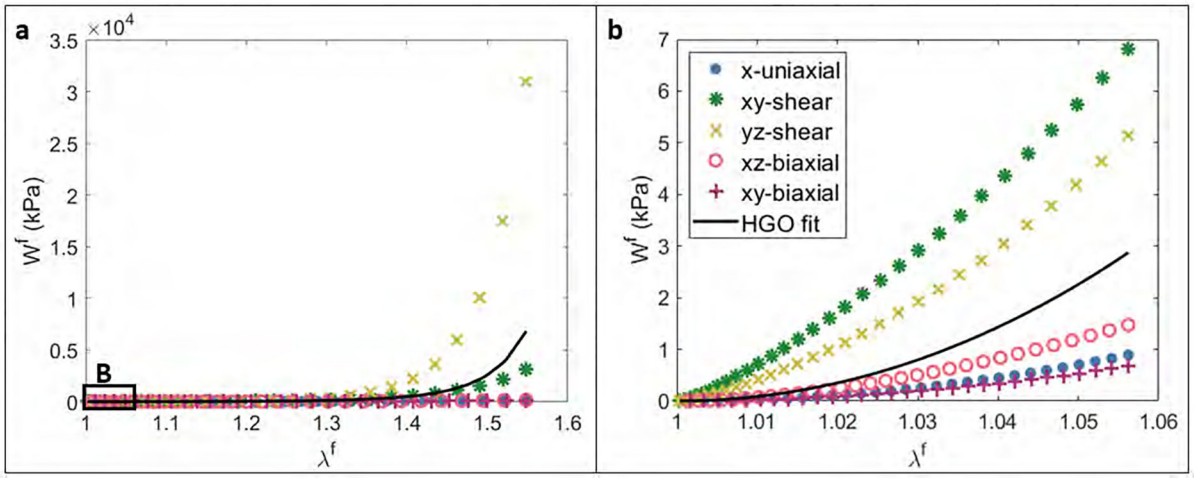

Fig. 5.

Holzapfel-Gasser-Ogden material property determination from microstructural networks under varied deformations for **a.** 112% Green strain, **b.** 10% Green strain

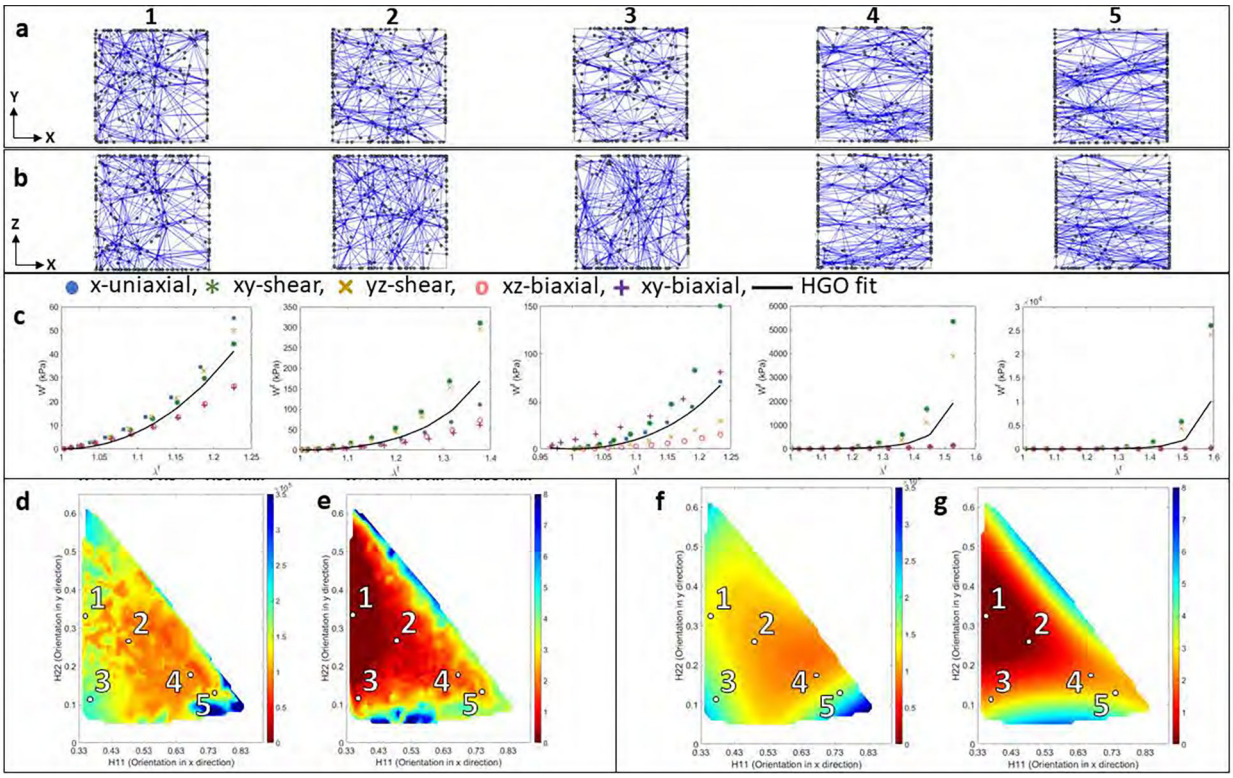

Fig. 6.

a1–5. xy view of networks 1–5. **b1–5** xz view of networks 1–5. **c1–5.** W^f-λ^f of networks 1–5 with alignment, network 1: H_{11}= 0.35 and H_{11}= 0.32, network 2: H_{11}= 0.5 and H_{11}= 0.32, network 3: H_{11}= 0.36 and H_{11}= 0.12, network 4: H_{11}= 0.66 and H_{11}= 0.18, network 5: H_{11}= 0.74 and H_{11}= 0.14. **d** and **e.** Contour plots of HGO material property, C_2 and C_3, respectively, as a function of alignment in x, H_{11}, and y direction, H_{22}. **f** and **g.** Contour plots of fitted value of HGO material property, C_2 and C_3, respectively, to the multivariate nonlinear model of Eq. 11

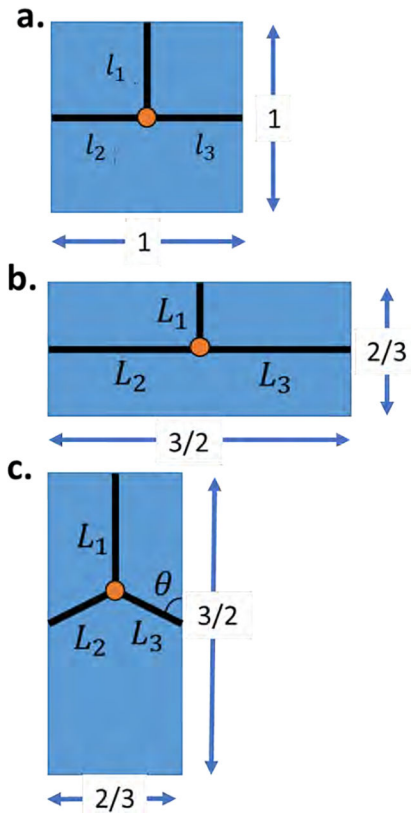

Fig. 7.

a. Undeformed network where $l_1 = l_2 = l_3 = l = 1/2$. **b.** Network stretched in the direction of strongest alignment where $L_2 = L_3 = 3/4$ and $L_1 = 1/3$. **c.** Network stretched transverse to the direction of stongest alignment where $L_2 = L_3$.

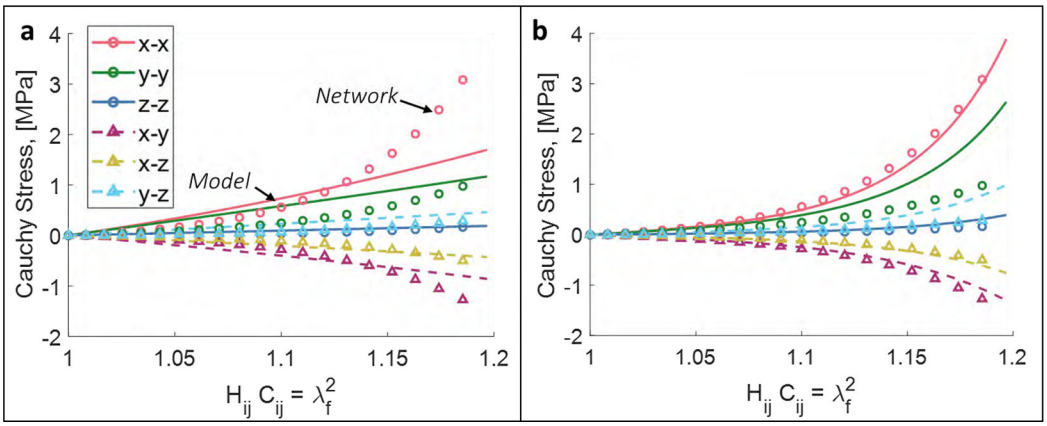

Fig. 8.

Comparison between HGO model and network simulation under complex deformation for **a.** initial fit and **b.** refit

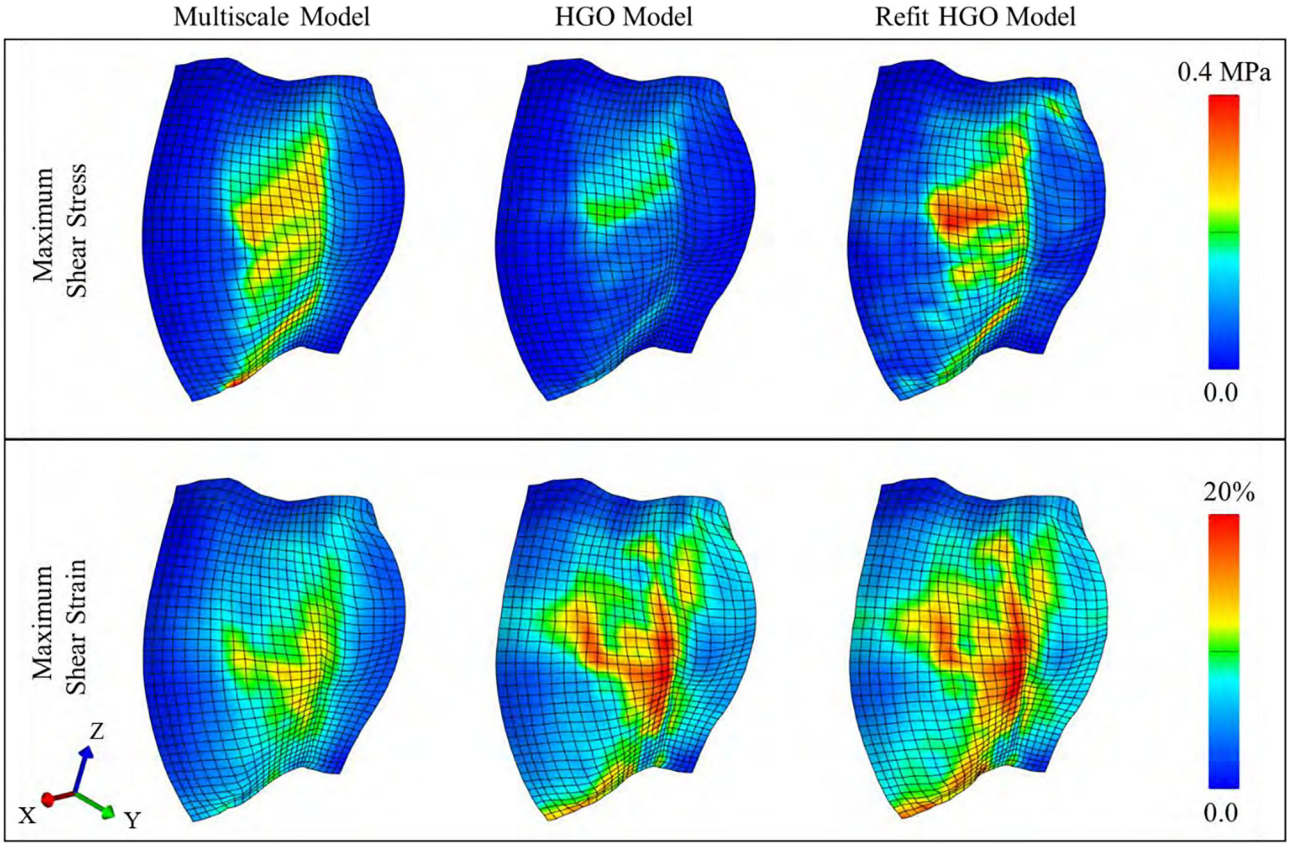

Fig. 9.

Maximum Shear Stresses and Strains of the multiscale, HGO, and refit HGO models for a single representative FCL sample during spinal flexion. The HGO model predicted the location of high shear stresses and strains while the refit HGO model improved the accuracy of magnitude of the maximum shear stress

Table 1.

Coefficients for the fit of HGO parameters C_2 and C_3

ij	a_{ij} [MPa]	β_{ij} [−]
00	1.56 ± 0.22	−11.84 ± 4.46
01	−8.30 ± 1.89	94.49 ± 28.61
10	14.10 ± 3.77	70.46 ± 15.98
11	−5.56 ± 0.58	−517.60 ± 97.80
02	33.70 ± 7.63	−106.90 ± 29.40
20	−59.90 ± 16.27	−59.44 ± 13.25
12	5.47 ± 0.79	474.80 ± 69.40
21	−35.90 ± 7.57	396.00 ± 75.60
22	67.25 ± 17.50	0

Table 2.

Computation Time for Multiscale vs HGO FE model

	Multiscale	**HGO**
Task	**Time [CPU hour]**	
Initial Simulation and Fit of 900 Networks (× 5 deformations × 20 steps)	NA	1.12
Re-simulation and Refit of 900 Networks (× 1 deformation × 20 steps)	NA	0.34
FE Simulation	2622.69	0.02
Total	2622.69	1.48